Barrier and internal wave contributions to the quantum probability density and flux in light heavy-ion elastic scattering

F. Brau and F. Michel*
Faculté des Sciences, Université de Mons-Hainaut, B-7000 Mons, Belgium

G. Reidemeister
Physique Nucléaire Théorique et Physique Mathématique, Université Libre de Bruxelles, CP229, B-1050 Bruxelles, Belgium
(Received 17 October 1997)

We investigate the properties of the optical model wave function for light heavy-ion systems where absorption is incomplete, such as $\alpha+{}^{40}$Ca and $\alpha+{}^{16}$O around 30 MeV incident energy. Strong focusing effects are predicted to occur well inside the nucleus where the probability density can reach values much higher than that of the incident wave. This focusing is shown to be correlated with the presence at back angles of a strong enhancement in the elastic cross section, the so-called ALAS (anomalous large angle scattering) phenomenon; this is substantiated by calculations of the quantum probability flux and of classical trajectories. To clarify this mechanism, we decompose the scattering wave function and the associated probability flux into their barrier and internal wave contributions within a fully quantal calculation. Finally, a calculation of the divergence of the quantum flux shows that when absorption is incomplete, the focal region gives a sizable contribution to nonelastic processes. [S0556-2813(98)04903-6]

PACS number(s): 25.70.Bc, 25.55.Ci, 24.10.Ht

I. INTRODUCTION

A better understanding of nucleus-nucleus collision dynamics has been achieved in the past few years by investigating light ion and light heavy-ion systems whose scattering is not dominated by strong absorption [1]. When strong absorption dominates the scattering—the most common situation—the scattering is known to be sensitive to the interaction potential in the extreme surface region only, around the so-called strong absorption radius [2]. In contrast, systems that display incomplete absorption have been found to carry information on conditions prevailing at much smaller distances. This information is contained in the large-angle region [3], as ''anomalous large angle scattering'' (ALAS) features at low energy [4] and clear rainbow scattering signatures when energy increases [5]. Very small absorption is not a prerequisite to the occurrence of these phenomena; indeed even in exceptional cases such as α-particle scattering from ^{16}O or ^{40}Ca, the absolute value of the low-ℓ S-matrix elements above 30 MeV incident energy is of the order of 10 percent [6,7].

Although the optical model provides a satisfactory account of many experimental data, including those displaying ALAS, one is often left with a ''black box'' description, where the link between the model parameters and the calculated cross sections is rather obscure. In the early days of the optical model, calculations of the full scattering wave function $\psi(\boldsymbol{r})$ and the associated quantum flux $\boldsymbol{j}(\boldsymbol{r})$ were carried out by McCarthy and by Amos [8–12] in order to investigate the scattering properties of the potential. Among other results, these calculations revealed the importance of focusing effects in systems such as nucleon-nucleus, where absorption is weak [8,10]. The importance of the focus in building up of a backward peak in some transfer reactions involving protons in the entrance or exit channel was also pointed out by Kromminga and McCarthy [13]. In the case of α-particle scattering, where absorption is stronger, it was found at that time [9] that, even when it could be discerned in the far side region, such a focusing effect has a negligible influence on the scattering, since propagation of the flux out of the nuclear medium leads to a nearly complete extinction of this contribution. Moreover, not much physical significance was attributed to the scattering wave function inside the nuclear volume, since the status of the optical model potential for composite particle scattering was then still very obscure. Surprisingly enough, few calculations of this type were reported subsequently in the literature; they have however been revived now and then in various contexts [14–17].

One obvious drawback of this type of approach is that the scattering wave function, and derived quantities like the quantum flux, contain contributions from all the mechanisms that are possibly active in the scattering system under study. Therefore many techniques have been developed to try to understand particular features observed in the cross sections in more familiar terms. Semiclassical approaches (as in Ref. [3] and references therein) have played a key role in this respect, even for systems where the applicability of these methods could seem problematic. Concepts like rainbow or glory scattering, orbiting and spiral scattering [18], nearside and farside [19], or internal wave and barrier wave contributions [20], have thus become commonplace in the optical model literature. One is thus led to the somewhat paradoxical situation where, although numerically exact results can be obtained from the formalism, the latter often contains less useful information than approximate solutions.

The philosophy of many of these approaches is to decompose the scattering amplitude into several subamplitudes

*Electronic address: michel@umh.ac.be

with, hopefully, simpler properties. For example, in one of these approaches [19,21], the elastic scattering amplitude is decomposed into the so-called nearside and farside amplitudes. The cross sections corresponding to each of these contributions are generally smooth, and their interference explains the Fraunhofer diffractive oscillations seen in various heavy-ion elastic scattering angular distributions. In another approach [20], the scattering amplitude is decomposed into its barrier and internal components. In contrast to the previous method, this approach works best at low energies, where the effective potential displays for each active partial wave (provided the nuclear potential is deep enough) a potential pocket separated by a barrier from the external region. This approach has explained how the anomalous features (ALAS) observed in elastic scattering for some light-ion systems emerge from an optical model description when the real part of the potential is deep and absorption is particularly low [3]; in particular, it has definitely settled the surprising fact that, in admittedly exceptional cases, part of the incident flux can remain in the entrance channel after a deep excursion into the nuclear medium.

The information obtained from semiclassical approaches can sometimes be obtained by resorting to purely quantal methods. For example, it has been shown that the semiclassical barrier-internal wave decomposition of the elastic scattering amplitude by Brink and Takigawa [20], initially carried out within a WKB approximation context, could be performed by resorting to ordinary optical model calculations [6]. In its simplest version, the technique consists in enhancing artificially the absorptive potential in the inside region of the potential, in order to make the internal wave contribution negligibly small, which provides the barrier wave contribution; the latter is subsequently subtracted from the full amplitude to calculate the internal wave component. An advantage of this approach is to provide—in contrast to the semiclassical calculations whose basic ingredients are action integrals evaluated between the active turning points [3,20]—wave functions corresponding to the different contributions to the scattering amplitude.

In view of the importance of a better understanding of the mechanisms underlying light ion and light heavy-ion scattering, we have reinvestigated the properties of the elastic scattering wave function and the associated quantum flux for a few light-ion systems. Our results can be summarized as follows. In all cases we have studied, focusing effects are indeed observed at low energy. When absorption is incomplete, focusing can become very strong and the probability density at the focus is found to reach values much larger than that of the incident wave—in some cases even larger than the values reported by McCarthy [8,10] and by Amos [11] for low energy nucleon scattering. The presence of the focus, which is located well inside the nuclear medium at low energy, is then found to be correlated with the occurrence at large angles of an internal wave contribution that dominates the scattering in the backward hemisphere and is responsible for the ALAS phenomenon. This is clearly demonstrated by examining the properties of the internal wave contribution to the total wave function. This focus thus appears to be the region of the nuclear medium from which most of the internal wave contribution to the elastic scattering cross section originates when absorption is incomplete.

As energy increases, the focus is found to move away from the center towards the far side of the nucleus; accordingly the flux that is refracted at back angles decreases—an effect which is enhanced by the increase of absorption with energy—and glory scattering is progressively replaced by rainbow scattering.

On the other hand, the calculation of the divergence of the quantum flux, which indicates where absorption is most effective, shows that the latter occurs in two distinct regions: in the surface region on the illuminated side of the nucleus, and, further inside the nucleus, around the focal point. For strongly absorbing systems, the first mechanism is clearly dominant, in accordance with the models generally used in direct nuclear reactions calculations which locate most of the coupling strength in the surface of the target nucleus, while for systems displaying reduced absorption, the second mechanism is significantly enhanced.

This paper is organized as follows. In Sec. II, we compare probability densities calculated for several optical model potentials, both for systems presenting reduced or strong absorption, as well as the associated quantum probability fluxes; we also investigate the energy dependence of the focusing properties of these potentials. In Sec. III, we decompose the scattering wave functions into barrier and internal wave components, thus obtaining the contribution of these two components to the probability density and the probability flux for these systems; the importance and localization of absorption are studied by calculating the barrier and internal wave contributions to the divergence of the quantum flux. A summary is presented in Sec. IV.

II. FOCUSING PROPERTIES OF OPTICAL POTENTIALS

A. A historical perspective

The measurement of low-energy elastic α-particle scattering up to large angles has disclosed the existence, for a few light targets like ^{16}O [7,22] and ^{40}Ca [4,23], of anomalous features in the angular distributions: whereas in many cases the angular distributions remain diffractive over the whole angular range, a large rise of the cross section is observed at back angles for these targets; around 30 MeV incident energy, this rise can exceed the Rutherford cross section by two to three orders of magnitude. When the energy increases, this backward rise, termed ALAS, disappears progressively and is replaced around 100 MeV incident energy by a rainbow behavior.

It was found that these anomalous features, which were long thought to lie outside the capabilities of an optical model description, can be reproduced quantitatively by using optical potentials with an imaginary part distinctly weaker than that used for ''normal'' systems and with a real part described by a conveniently chosen form factor [24,4,7]. It was soon realized that the existence of a backward rise in the cross section is due to part of the incident wave that crosses the effective potential barrier and reemerges after having been reflected at the innermost turning point [20], and thus that, contrary to what had been considered to be a general rule, elastic scattering of composite particles like the α-particle is not necessarily governed by strong absorption. An important consequence of this unexpected transparency is that the experimental elastic scattering cross sections carry

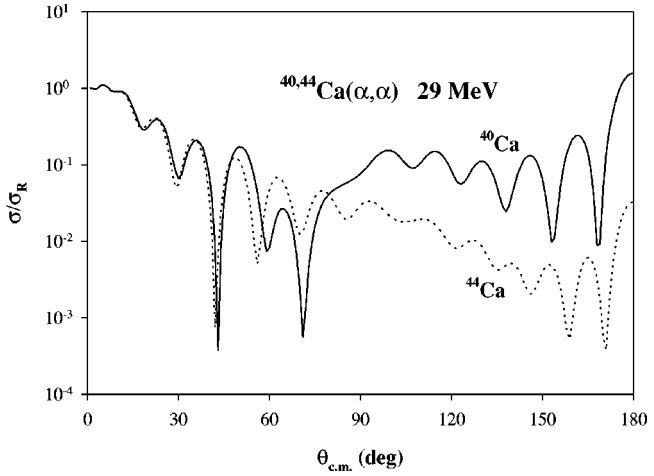

FIG. 1. Comparison of the optical model elastic scattering differential cross sections (normalized to the Rutherford cross section) for the $\alpha+{}^{40}$Ca (full line) and $\alpha+{}^{44}$Ca (dotted line) systems at 29 MeV incident energy.

information on the interaction potential well inside the strong absorption radius. Indeed, a consistent study of the phenomenon on a broad energy range makes possible extraction of an unambiguous global optical potential whose real part is definitely deep and is well defined up to fairly small distances [23,7].

These potentials were later shown to contain more than a simple parametrization of the cross sections. Indeed the properties of the phenomenological $\alpha+{}^{16}$O global optical potential were shown [7,25] to be compatible with microscopic approaches such as resonating group method (RGM), which take into account antisymmetrization effects between projectile and target in an exact way. In particular, the numerous unphysical states, which are bound by the deep phenomenological potentials below the threshold, were shown to be close analogues of the so-called forbidden states of the RGM, and must thus be discarded [26]. One is thus led to give credibility to the wave functions associated with the deep local potentials obtained from analyses of elastic light-ion scattering down to small distances, the more so as the effects of nonlocality on the wave function (the so-called Perey effect) are known to be small for low-mass projectiles [26].

B. Comparison between strong absorption and reduced absorption

As a starting point, we investigate the properties of two optical potentials [6] describing α-particle scattering from targets of comparable masses at the same incident energy, that is, ^{40}Ca and ^{44}Ca at 29 MeV. The main difference between these two systems lies in the strength of the absorption needed for describing the data: whereas α particles scattered from ^{44}Ca are strongly absorbed and the angular distribution displays a diffractive behavior up to large angles, the $\alpha+{}^{40}$Ca system is characterized by an incomplete absorption and a spectacular backward enhancement. The angular distributions calculated with these two potentials, which give a good description of the experimental angular distributions over the whole angular range, are contrasted in Fig. 1.

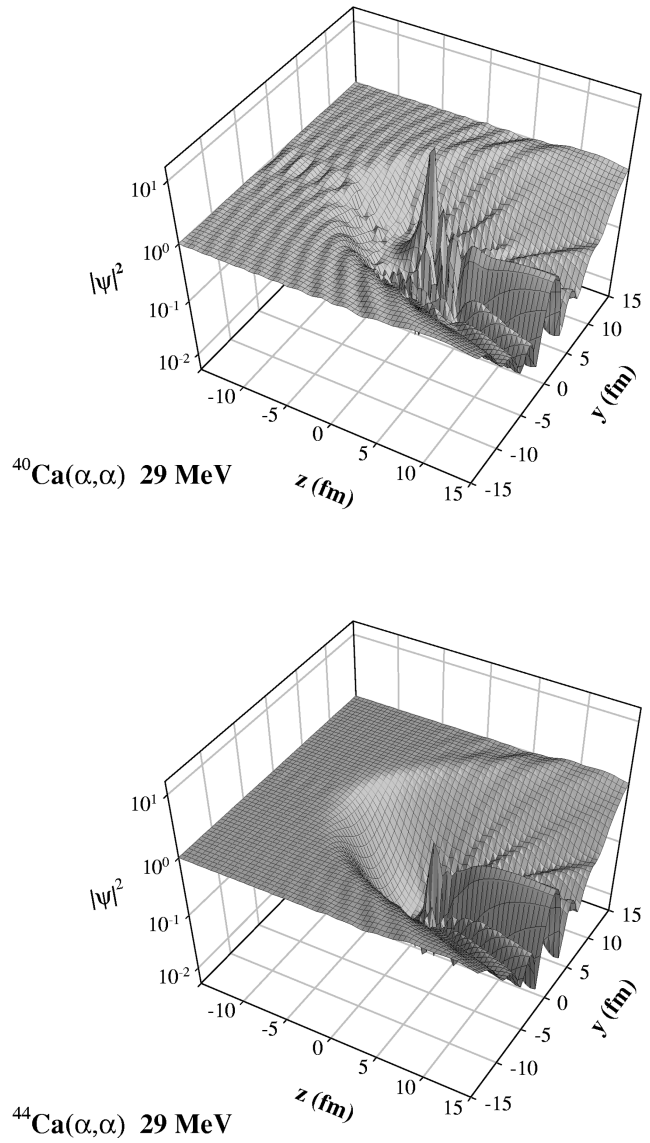

FIG. 2. Probability densities associated with the two optical model potentials used in Fig. 1. In this and similar figures, the incident beam comes along the negative z axis and the probability density has been normalized to 1 for large negative z values.

The probability densities $\rho(\boldsymbol{r})=|\psi(\boldsymbol{r})|^2$ associated with these two optical potentials are displayed in Fig. 2 and are seen to be generally similar. In particular, the ''parabolic cup'' surrounding the interaction region is essentially a Coulomb effect. In the forward direction, the structures observed for the two systems are also nearly identical outside the interaction region. This is not so at larger angles: one observes the appearance of ripples on the illuminated side of the ^{40}Ca nucleus in several preferred directions, especially around $\theta=180°$, which (as shown later) are due to an internal wave contribution to the scattering, whereas the $\alpha+{}^{44}$Ca probability density is essentially flat on the illuminated side. Moreover, a strong focusing effect is seen to be present behind the center of the nucleus in the ^{40}Ca case, whereas it is barely visible in ^{44}Ca. (Note the use of a logarithmic scale in the figure.) This focus is followed at larger distances by a broad ridge whose importance is seen, in contrast, to be barely affected by absorption.

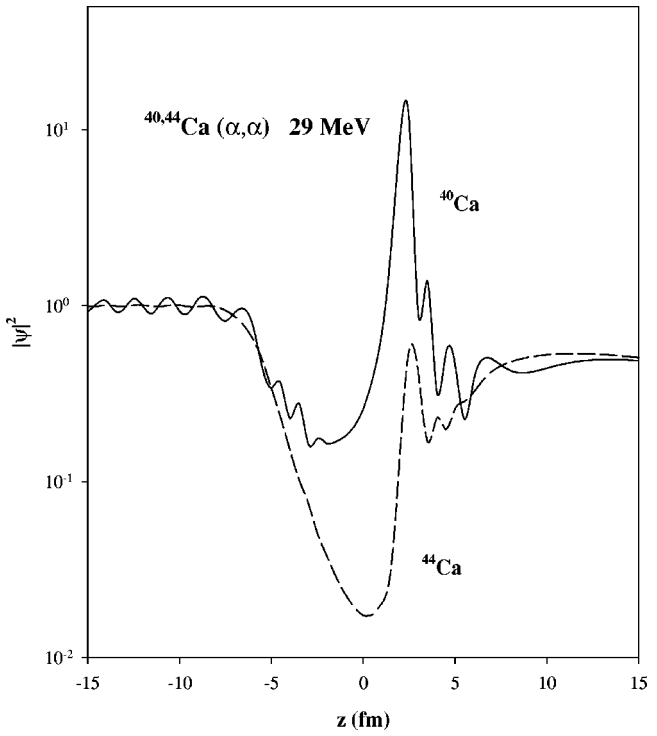

FIG. 3. Comparison of the $\alpha+{}^{40}$Ca and $\alpha+{}^{44}$Ca probability densities at 29 MeV along the axis of the incident beam.

To give a more quantitative impression of these effects, we present in Fig. 3 a section of the probability densities along the axis of the incident beam (z axis). It is clearly seen that the focus is localized well inside the interaction region, at about 2 fm from the center of the target nucleus. This behavior is similar to that reported by McCarthy in his analysis of low-energy neutron scattering [8,10]. Whereas the magnitude of the peak at the focus in the ^{44}Ca case is lower than that of the incident wave, it reaches about 20 times that value in the ^{40}Ca case. In contrast, the broad ridge alluded to above is seen to develop mainly outside the interaction region. Finally, the oscillations observed on the illuminated side of the ^{40}Ca nucleus, which will be shown to be related to the internal wave contribution to the scattering, are seen to be strongly suppressed in ^{44}Ca.

C. Quantum probability flux and classical trajectories

To understand better the origin of the features seen in the density plots, we calculated the quantum flux

$$\boldsymbol{j}(\boldsymbol{r}) = \frac{\hbar}{\mu}\mathrm{Im}(\psi^*(\boldsymbol{r})\boldsymbol{\nabla}\psi(\boldsymbol{r})) \tag{1}$$

associated with the total wave function $\psi(\boldsymbol{r})$ for the two cases presented above (Figs. 4 and 5). For large impact parameters the incident flux does not penetrate into the nuclear interaction region and one observes a bunching of the streamlines at the edge of the parabolic cup mentioned above, which is clearly associated with the Coulomb interaction. For smaller impact parameters, the streamlines are progressively pulled towards the nuclear center and the flux vectors are seen to converge to a region located near the focus observed in the probability density. Whereas the flux density

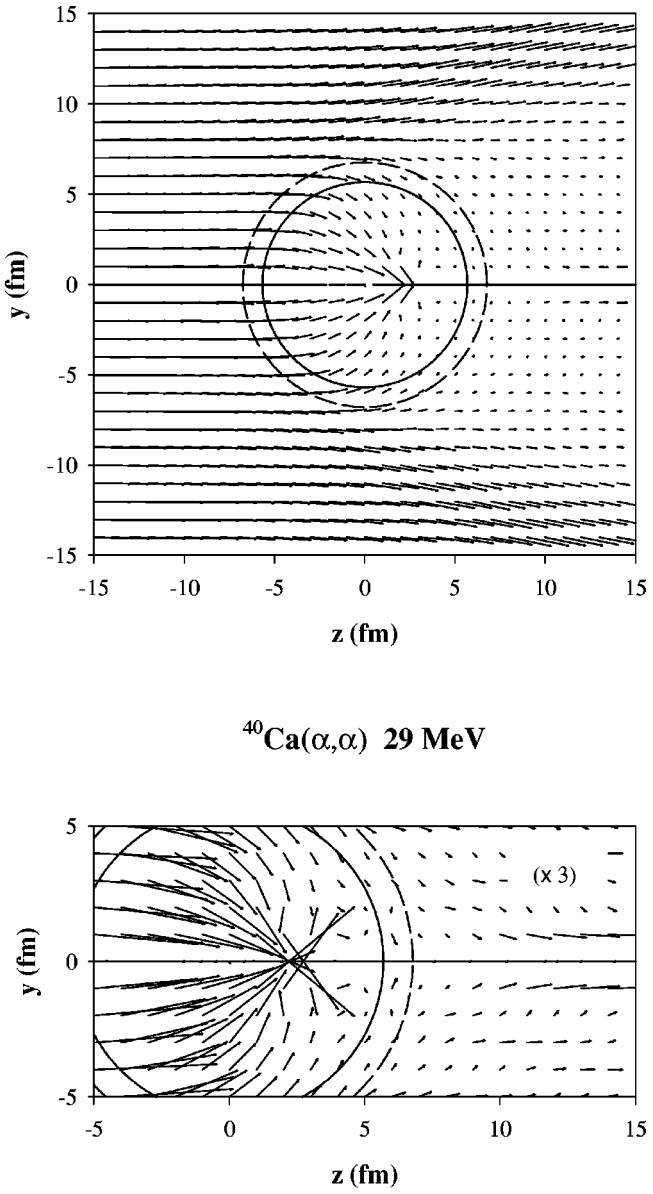

FIG. 4. Quantum probability flux associated with the 29 MeV $\alpha+{}^{40}$Ca scattering wave function (arbitrary units); in the lower part of the figure, which presents an enlargement around the focal point, the flux has been multiplied by a factor of 3. The full-line and dashed-line circles represent the distances where the real and the imaginary parts of the optical potential have a depth equal to one tenth of their central values.

is seen to be rapidly damped on its way towards the focus in the ^{44}Ca case, and as a result the intensity at the focus remains rather small, in the ^{40}Ca case this intensity is seen to increase significantly, reaching a much higher value at the focus.

Unfortunately, it is difficult to obtain more insight from this figure, because the flux calculated here includes both the incident wave and the scattered wave contributions.

As was shown by McCarthy in his pioneering calculations, the classical trajectories are useful for investigating qualitatively the focusing properties of the potential, provided the incident energy is not too low [8]. The classical trajectories associated with the real part of the 29 MeV ^{40}Ca potential for a few impact parameters are shown in Fig. 6. It

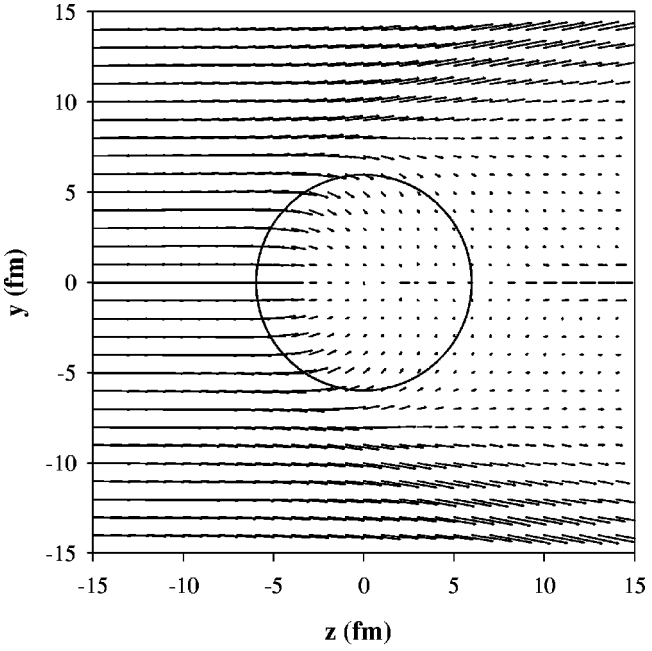

^{44}Ca(α,α) 29 MeV

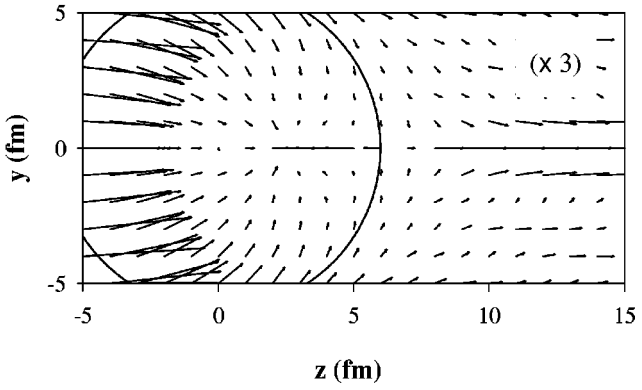

FIG. 5. Same as Fig. 4 for the 29 MeV $\alpha+{}^{44}$Ca system; for that system the real and imaginary radii, as defined in Fig. 4, are nearly equal.

is seen that the trajectories with an impact parameter less than about 6 fm converge in a precise way to a point located very near the quantum focus. These classical trajectories are identical to the rays which would be calculated in a geometrical optics context using the position-dependent refractive index

$$n(r)=\sqrt{1-\frac{V(r)}{E_{\text{c.m.}}}} \tag{2}$$

where $V(r)$ denotes the real part of the optical potential.

The refractive index near the origin for the incident energy and potential considered here is comparable to that of diamond for ordinary light, that is about 2.5; this is why focusing occurs inside the refracting sphere at low energy. When the energy increases, Eq. (2) predicts a decrease of the refractive index; in this simple picture the focus is thus expected to shift away from the nuclear center as energy increases, if one assumes that the potential depth is energy independent (which is indeed the case in a first approximation), a feature already observed by McCarthy in his calculations.

^{40}Ca(α,α) 29 MeV

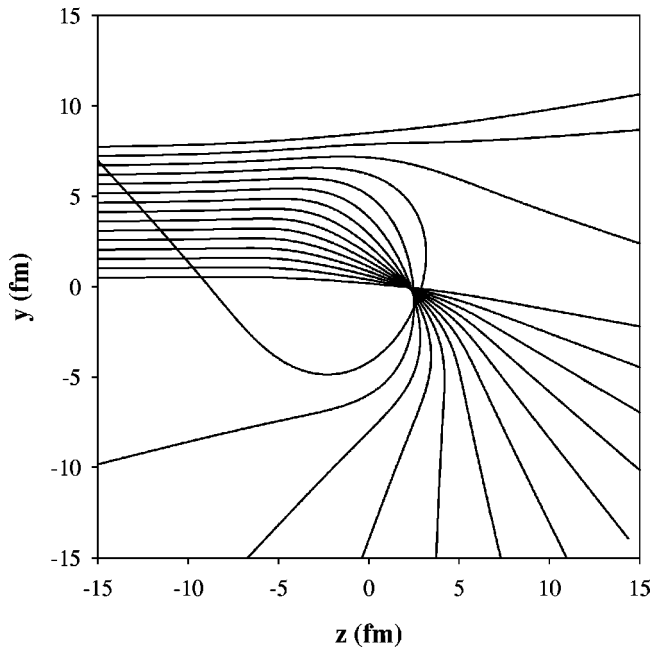

FIG. 6. Classical trajectories for the $\alpha+{}^{40}$Ca system at 29-MeV incident energy.

D. Energy dependence of the focusing properties of the potential

To conclude this tour of the focusing properties of the α-nucleus optical potential, we examine the energy behavior of the probability densities. We concentrate here on another transparent system which has played a key role [7,26] in understanding the dynamics of the α-nucleus interaction, the $\alpha+{}^{16}$O system. The parameters used are those of the global optical potential in Ref. [7]. As is seen in Figs. 7 and 8, the focus moves away from the illuminated side of the nucleus when energy increases, and the density at the focus decreases steadily. These properties are easily understood if one takes into account the fact that the real potential depth at small distances decreases slowly with energy, ranging from about 160 MeV to 120 MeV when the incident energy increases from 30 to 150 MeV [7], while absorption increases regularly in this range. The refractive index in Eq. (2) thus also decreases with energy; for ^{16}O(α,α) scattering, it varies from about 2.7 to 1.4 over the same energy range and the focal length of the system increases accordingly. It is interesting to note that the region of the potential to which the scattering is most sensitive, which was obtained in Ref. [7] from a notch test analysis, coincides with the location of the focus at low energy.

Above about 60 MeV, we found that the low angular momentum classical trajectories are still converging to a focus inside the target nucleus but, contrary to the example

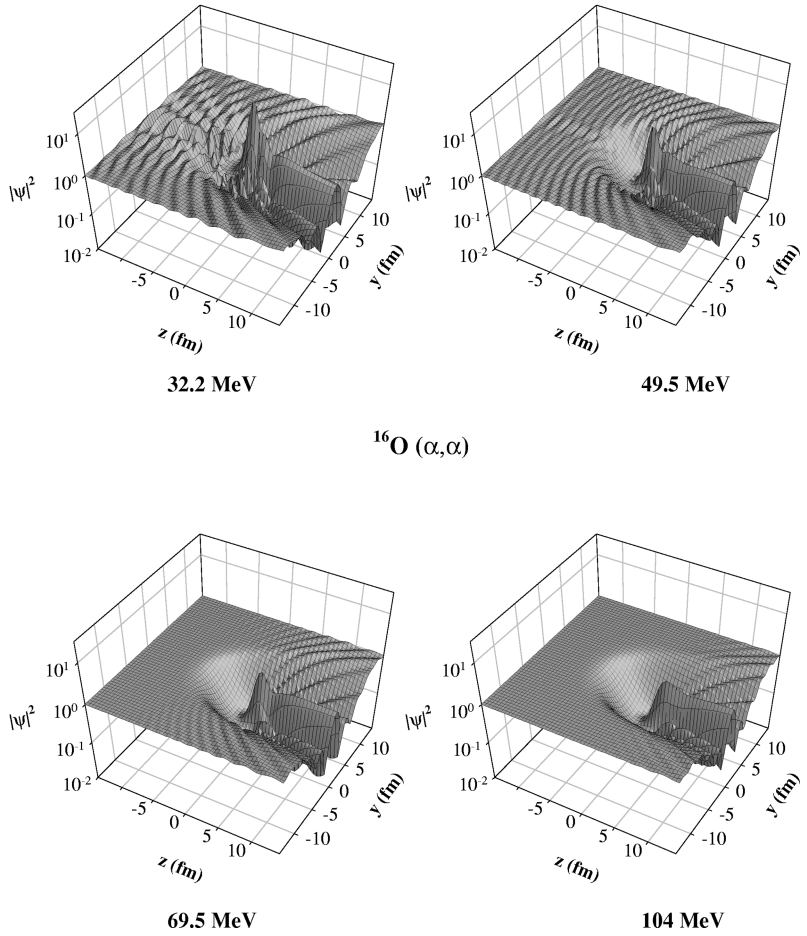

FIG. 7. Evolution with energy of the probability density for the $\alpha+{}^{16}$O system between 32.2 and 104 MeV.

displayed in Fig. 6, they are not deflected beyond some critical angle that decreases with energy. Accordingly, ALAS is progressively replaced by a rainbow behavior and the ripples that were still clearly observed on the illuminated side of the target at 32.2 and 49.5 MeV are seen to have completely disappeared by 69.5 MeV as a result of the disappearance of the internal wave contribution to the scattering beyond this energy.

III. BARRIER-INTERNAL WAVE DECOMPOSITION OF THE WAVE FUNCTION

A. The barrier and internal wave contributions to elastic scattering

In order to clarify the focusing properties of the nuclear potentials, we have decomposed the elastic scattering wave function into two contributions, corresponding respectively to the part of the incident flux reflected at the barrier of the effective potential and the part that penetrates the nuclear interior. This decomposition makes sense for the systems studied here at low energy, since the effective potentials have a pocket for all the active partial waves. It must be stressed that in the original semiclassical internal-barrier wave decomposition of Brink and Takigawa [20], this decomposition was not performed on the scattering wave function but on the scattering amplitude $f(\theta)$, making possible the calculation of ''barrier'' and ''internal wave'' contributions $f_B(\theta)$ and $f_I(\theta)$ to $f(\theta)$, and thus of the contributions

$$\sigma_B(\theta)=|f_B(\theta)|^2, \quad \sigma_I(\theta)=|f_I(\theta)|^2 \tag{3}$$

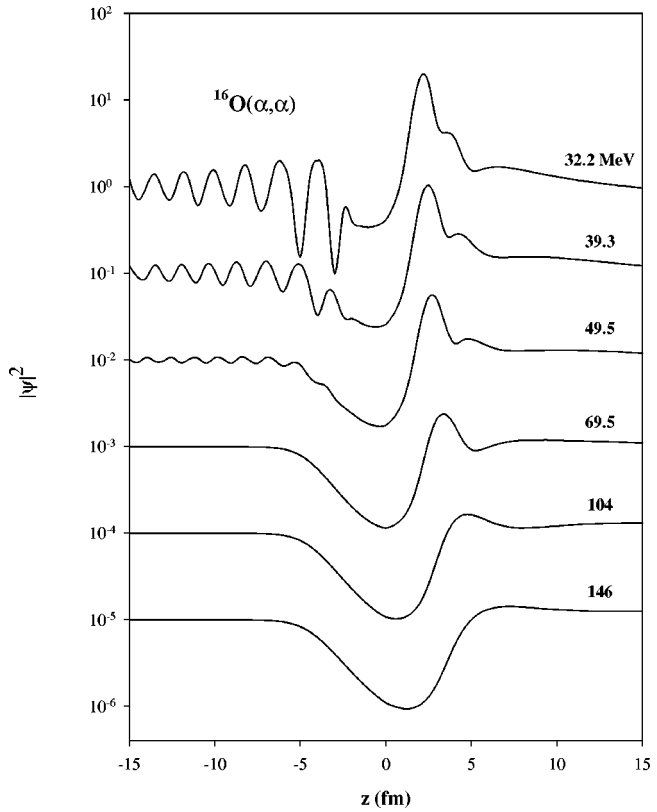

FIG. 8. Evolution with energy of the probability density along the incident beam axis for the $\alpha+{}^{16}$O system between 32.2 and 146 MeV.

to the full elastic scattering cross section $\sigma(\theta)$. More precisely, the elastic scattering matrix S_ℓ is written as [20]

$$S_\ell = S_{B,\ell} + S_{I,\ell} \tag{4}$$

where $S_{B,\ell}$ is given by

$$S_{B,\ell} = \exp(2i\delta_1^\ell)/N_\ell \tag{5}$$

and, if multiple reflections between the two inner turning points (that is, resonances in the potential pocket) are neglected, a condition which is met in most cases except possibly at very low incident energy, $S_{I,\ell}$ is given by

$$S_{I,\ell} = \exp(2i\delta_3^\ell)/N_\ell^2 \tag{6}$$

In Eq. (5), δ_1^ℓ is the usual WKB phase shift corresponding to the external turning point and N_ℓ measures the penetrability of the barrier of the effective potential $U_{\rm eff}^\ell$ for angular momentum ℓ; in Eq. (6), δ_3^ℓ is the WKB phase shift corresponding to the innermost turning point

$$\delta_3^\ell = S_{32}^\ell + S_{21}^\ell + \delta_1^\ell \tag{7}$$

where S_{ij}^ℓ denotes the semiclassical action integral for angular momentum ℓ, evaluated between the (complex) turning points $r_{i,\ell}$ and $r_{j,\ell}$

$$S_{ij}^\ell = \int_{r_{i,\ell}}^{r_{j,\ell}} dr \left\{ \frac{2\mu}{\hbar^2} [E_{\rm c.m.} - U_{\rm eff}^\ell] \right\}^{1/2}. \tag{8}$$

Finally, the full elastic scattering amplitude $f(\theta)$ is decomposed as [20]

$$f(\theta) = f_B(\theta) + f_I(\theta) \tag{9}$$

where the barrier wave and internal wave amplitudes, f_B and f_I, are given in conventional notation by

$$f_B(\theta) = f_R(\theta) + \frac{1}{2ik} \sum_\ell (2\ell+1) \exp(2i\sigma_\ell) \times [S_{B,\ell} - 1] P_\ell(\cos\theta), \tag{10}$$

$$f_I(\theta) = \frac{1}{2ik} \sum_\ell (2\ell+1) \exp(2i\sigma_\ell) S_{I,\ell} P_\ell(\cos\theta). \tag{11}$$

This decomposition, which requires the localization for each ℓ value of the active turning points and the evaluation of action integrals in the complex plane between these turning points, seems in principle to be restricted to analytical potentials. It was however shown in Ref. [6] that it can in fact be carried out in a fully quantal context, using scattering matrix coefficients supplied by any optical model code. The basic technique consists in enhancing artificially the absorption at small distances to enhance the imaginary part of S_{32}, in order to damp the internal wave contribution to the scattering amplitude and thus to provide the barrier wave contribution $f_B(\theta)$. The internal wave amplitude f_I is obtained in a second step by subtraction of f_B from the full scattering amplitude $f(\theta)$. The extra absorption used must of course be restricted to small distances in order to preserve both the external WKB phase shift δ_1^ℓ and the barrier penetration factor N_ℓ. Although, as explained in Ref. [6], this simple technique leads in most cases to good agreement with the full WKB calculation, it was found to lead sometimes to serious discrepancies, and therefore a more elaborate quantum mechanical scheme was devised in Ref. [6] in order to alleviate these problems. In the rest of the present paper, we will use the simpler technique described above, since for the cases examined here it proved quite stable and reliable.

An important byproduct of this technique is to provide, beyond the S-matrices S_B and S_I, wave functions ψ_B and ψ_I, defined even in the interaction region, associated with the barrier wave and internal wave contributions. Use of a conveniently enhanced absorption provides the barrier contribution ψ_B to the total wave function ψ, and the internal contribution ψ_I, which we define by

$$\psi = \psi_B + \psi_I \tag{12}$$

is thus obtained in a second step by subtraction of ψ_B from ψ.

Although fine details of the components of the wave function thus obtained depend somewhat on the exact prescription used for enhancing the absorption, we checked that—as far as the WKB component S-matrices are correctly reproduced—little uncertainty arises in our decomposition of the wave function.

B. Components of the wave function

We applied the technique described in the previous subsection to the ^{40,44}Ca(α,α) cases at 29 MeV. The potential parameters are still those of Ref. [6]; for the imaginary potential $\Delta W(r)$ needed to enhance absorption in the internal region, use was made of the same form factor as the perturbative potential used in that work, that is

$$\Delta W(r) = \Delta W_0 \exp[-(r/\rho)^4]. \tag{13}$$

As discussed in Ref. [6], an adequate choice of the parameter ρ guarantees that this form factor decreases sufficiently rapidly in the barrier region, a feature that is important to avoid unwanted modifications of the barrier contribution. A convenient choice is

$$\rho \approx R_B/2 \tag{14}$$

where R_B denotes the barrier radius at the grazing angular momentum. At the same time, this form factor decreases sufficiently smoothly so as not to introduce additional spurious turning points in the problem. The results of the calculation should not depend critically on these cutoff parameters; the values used here are $\Delta W_0 = -100$ MeV, $\rho = 3.25$ fm for the ^{40}Ca case, and $\Delta W_0 = -50$ MeV, $\rho = 3.40$ fm for the ^{44}Ca case.

The barrier wave and internal wave cross sections $\sigma_B(\theta)$ and $\sigma_I(\theta)$ corresponding to these two systems are compared in Fig. 9, together with the moduli of the corresponding S-matrix coefficients $S_{B,\ell}$ and $S_{I,\ell}$. One sees that, whereas the barrier wave contributions are remarkably similar for both systems (except for trivial size effects), the internal wave contributions to the S-matrix have the same cutoff angular momenta but differ by about one order of magnitude. Correspondingly, the internal wave cross sections are seen to differ by about two orders of magnitude, but they have a very similar pattern. The ALAS phenomenon observed in the

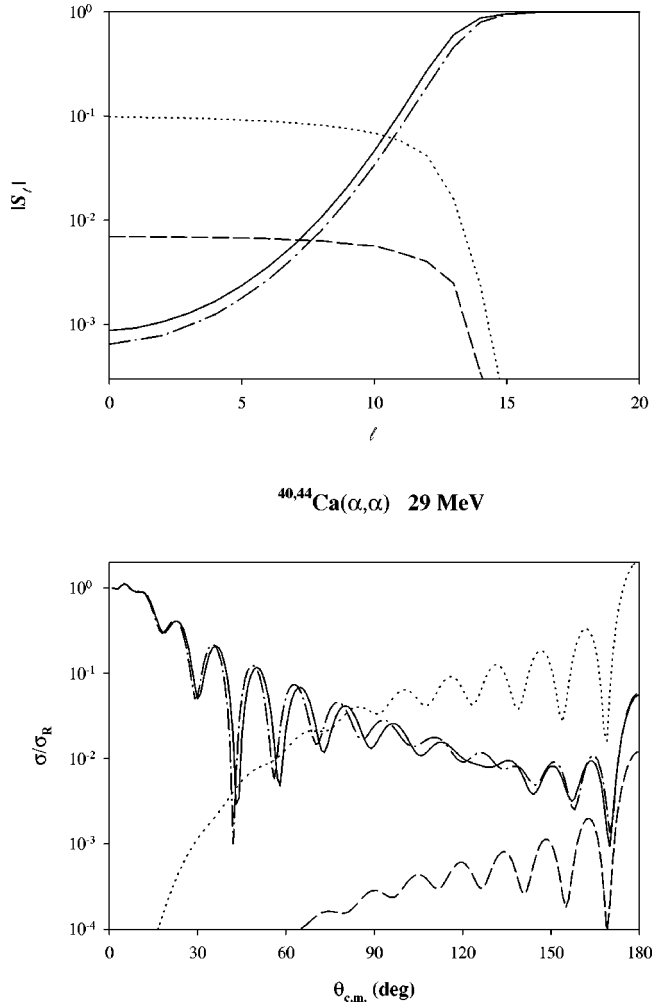

FIG. 9. Modulus of the internal and barrier wave S-matrix elements (upper part) and the corresponding differential cross sections (lower part) for $\alpha + {}^{40,44}$Ca elastic scattering at 29 MeV. (Internal wave contribution: ^{40}Ca, dotted line; ^{44}Ca, dashed line. Barrier wave contribution: ^{40}Ca, full line; ^{44}Ca, dot-dashed line.)

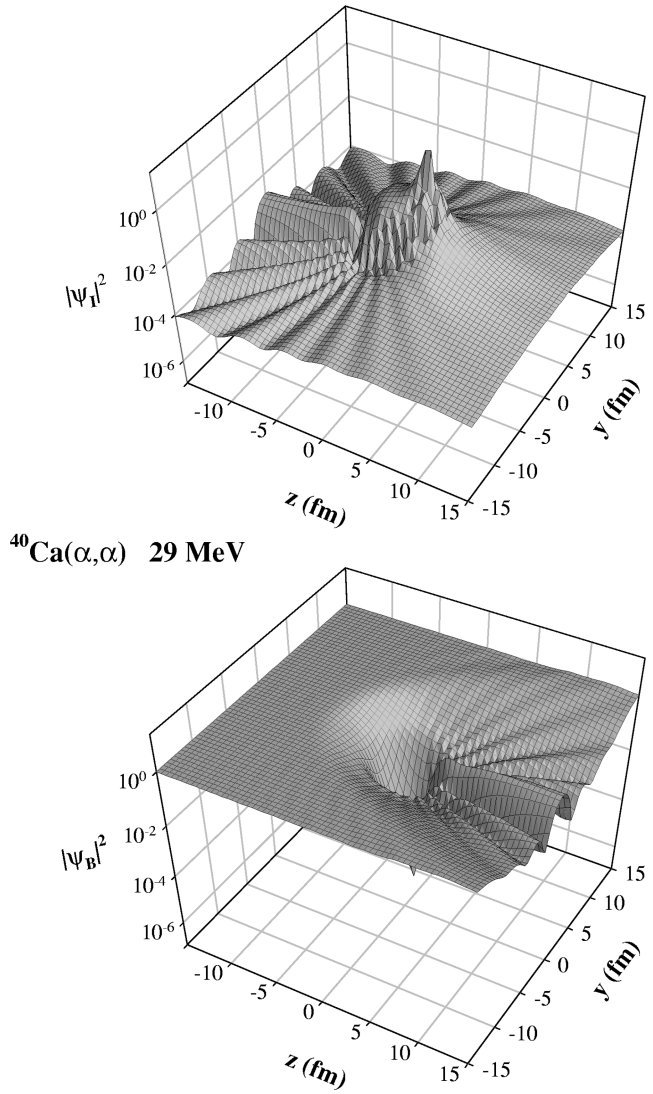

FIG. 10. Internal and barrier wave contributions to the probability density for the $\alpha + {}^{40}$Ca system at 29 MeV.

^{40}Ca case is thus seen to be entirely due to an enhanced internal wave contribution to the scattering, as was first established by Brink and Takigawa [20].

The very different role played by these two contributions is illustrated by the probability densities $|\psi_B|^2$ and $|\psi_I|^2$ obtained for the two systems, which are displayed in Figs. 10 and 11. Again the barrier probability densities are seen to be strikingly similar for both systems. We note in passing that the broad ridge observed in the very forward direction, which has a comparable importance in the two systems, and which should not be confused with the focus found inside the nucleus, is essentially a barrier phenomenon.

In contrast, while the internal probability densities have a very similar pattern, they differ by about two orders of magnitude. They both display a prominent peak located behind the center of the target, which coincides with the focus observed in the full scattering wave function (see Fig. 2); of course the ^{44}Ca focus is about two orders of magnitude lower than its ^{40}Ca counterpart. This peak is preceded on the illuminated side by a broad bump centered around the origin; the latter was not conspicuous in the full wave function because the barrier contribution is still important in this region. At larger distances, the internal density is seen to oscillate in the backward hemisphere; the angular positions of its maxima and minima coincide with those of the internal wave contribution to the cross section (Fig. 9), and thus with those of ALAS in the ^{40}Ca case (Fig. 1). A more quantitative comparison of the different components of the wave function along the axis of the incident beam can be found in Fig. 12.

One of the merits of our decomposition of the wave function is to display in a striking way the strong correlation between the existence of a focus inside the target nucleus and an internal wave contribution to the scattering cross section. When absorption dominates the scattering, a focus can still be discerned in the internal density, but its contribution to the total density is comparatively weak and its contribution to backward scattering is negligible. In contrast, in a context of incomplete absorption, the focus is found to play a leading role in the building up of the ALAS phenomenon observed in the backward angular distribution.

C. Components of the quantum flux

We have likewise calculated the quantum flux corresponding to each of the wave function components for the

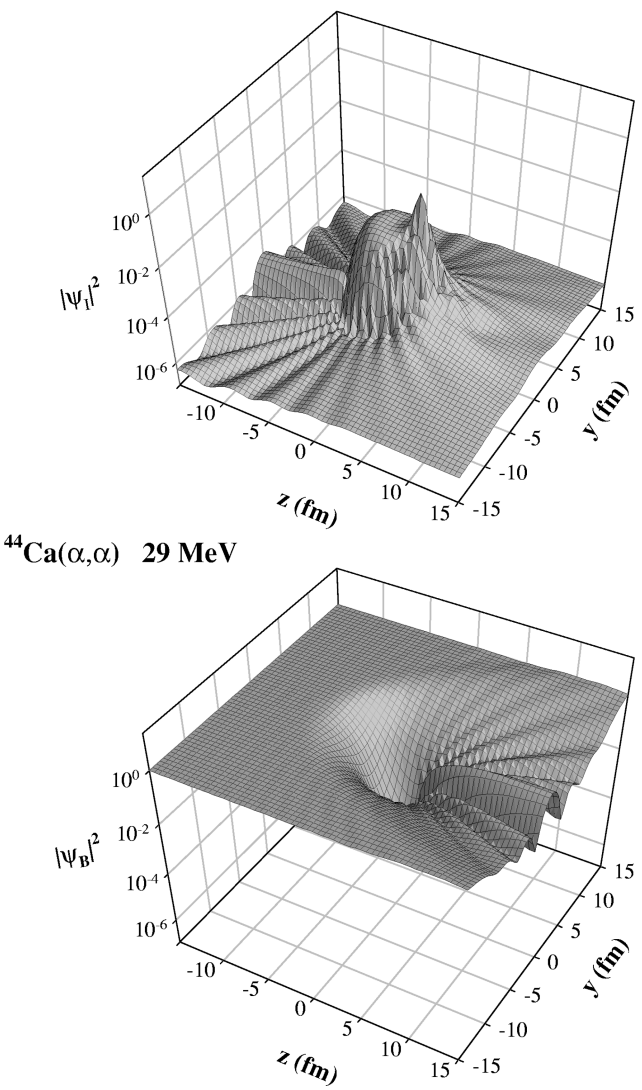

FIG. 11. Same as Fig. 10 for the $\alpha+{}^{44}$Ca system at 29 MeV.

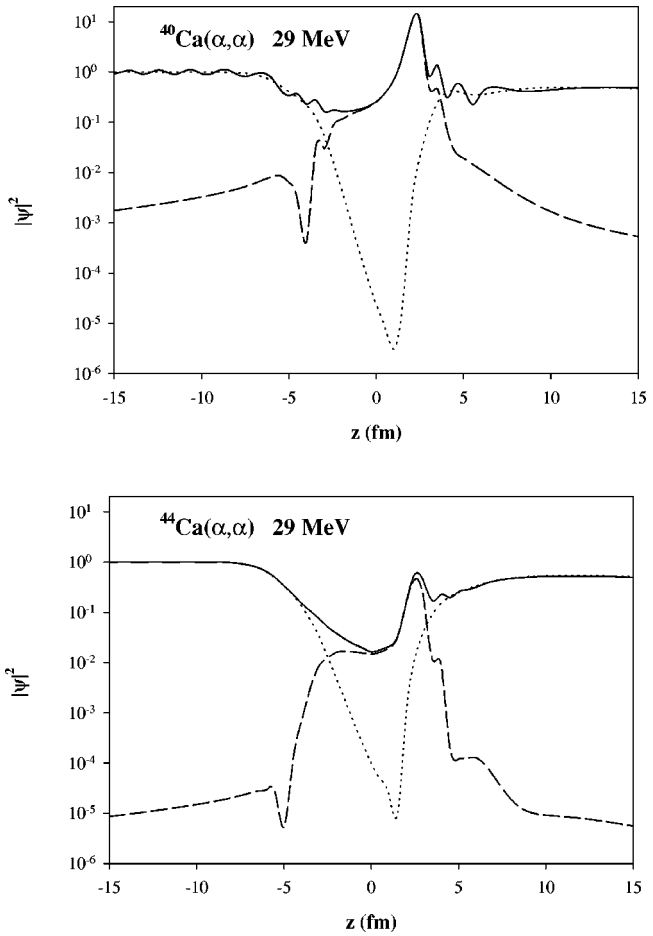

FIG. 12. Internal wave contribution (long dashed lines) and barrier wave contribution (dotted lines) to the total probability density (full lines) for the $\alpha+{}^{40}$Ca and $\alpha+{}^{44}$Ca systems at 29 MeV along the incident beam axis.

same two systems; these flux components, which will be denoted by $\boldsymbol{j}_B$ and $\boldsymbol{j}_I$, are calculated from Eq. (1) using the barrier or the internal component of the wave function. We note that $\boldsymbol{j}$ and $\boldsymbol{j}_B$, which both derive from wave functions satisfying a Schrödinger equation with an absorptive potential, have necessarily a negative divergence. This is not necessarily so for $\boldsymbol{j}_I$ since the equation for ψ_I, which reads

$$-\frac{\hbar^2}{2m}\nabla^2\psi_I+(V+iW)\psi_I-i\Delta W\psi_B=E\psi_I \qquad (15)$$

[where $V+iW$ is the original optical potential and ΔW is the extra absorption of Eq. (13)], is coupled to ψ_B.

For the $\alpha+{}^{40}$Ca system, we present in the lower part of Fig. 13 a closeup of the internal flux contribution in the focus region, which essentially confirms the features observed for the total flux in the lower part of Fig. 4 for that system. It is, however, interesting to notice that the rather peripheral current lines which bend towards the axis and contribute to the enhancement of the total wave function beyond 10 fm (see Fig. 4) are not present here and that they are thus clearly associated with the barrier wave function. On the other hand, we show in the upper part of Fig. 13 the internal flux contribution on a broader scale; it has been multiplied by a factor of 1000 in order to enhance its asymptotic behavior and has not been represented for distances lower than 6 fm, where it is much larger and would overflow the figure at this scale. The full line and dashed line circles represent the distance where the real and the imaginary parts of the optical potential have fallen to one tenth of their central values.

In Fig. 14, we finally display the barrier part of the quantum flux for ^{40}Ca(α,α) scattering; one sees in this figure how the current lines grazing the surface of the potential survive absorption to build up a sizeable contribution to the probability density in the forward direction along the axis of the incident beam. Calculations carried out for ^{44}Ca(α,α) scattering give a very similar picture for the barrier contribution to the flux. As expected, the internal wave contribution to the flux is found to be nearly negligible in the ^{44}Ca case, and is not represented here.

D. Divergence of the quantum flux

The divergence of the flux associated with the scattering wave function gives a measure of the localization of nonelastic collisions, which deplete the entrance channel. It is simply related to the probability density and to the imaginary part $W(r)$ of the optical potential used in the calculation by

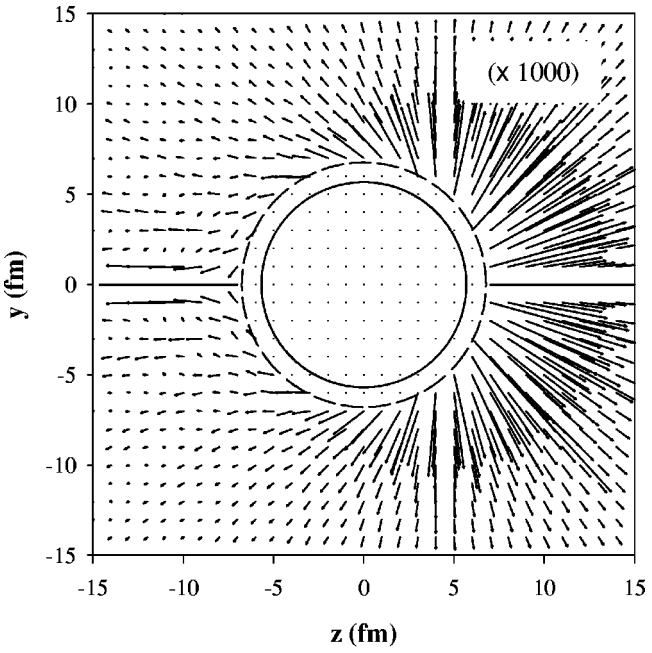

^{40}Ca(α,α) 29 MeV

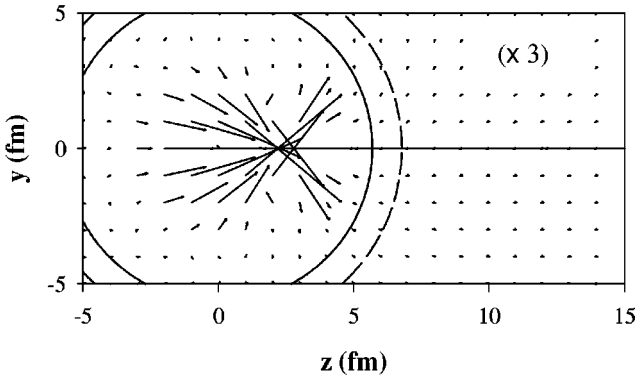

FIG. 13. Internal wave contribution to the probability flux for the $\alpha+{}^{40}$Ca system at 29 MeV. In the upper part, for clarity the flux in the central region ($r<6$ fm) has not been drawn. The lower part displays the same contribution around the focal point. In the upper (lower) part of the figure, the flux has been multiplied by a factor of 1000 (3) with respect to the upper part of Fig. 4.

$$\nabla\cdot\boldsymbol{j}(\boldsymbol{r})=\frac{2}{\hbar}W(r)|\psi(\boldsymbol{r})|^2 \tag{16}$$

which is easily derived from the definition of the flux [Eq. (1)] and from the Schrödinger equation.

The results obtained for the $\alpha+{}^{40}$Ca and $\alpha+{}^{44}$Ca systems are presented in Fig. 15. Inspection of this figure reveals two contributions to the divergence of the flux. The first is localized at the outskirts of the potential and has its maximum on the illuminated side of the target. The second one is located near the focus, much deeper inside the potential and is distinctly much larger in the $\alpha+{}^{40}$Ca case. One should of course not forget, before making any statement about the relative importance of these various contributions, that integration in three dimensions introduces the factor

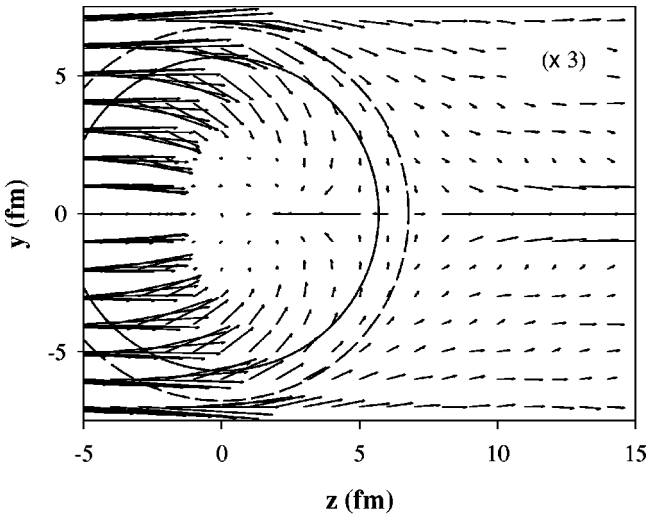

^{40}Ca(α,α) 29 MeV

FIG. 14. Barrier wave contribution to the probability flux for the $\alpha+{}^{40}$Ca system at 29 MeV. The flux has been multiplied by a factor of 3 with respect to the upper part of Fig. 4.

$r^2\sin\theta$ and will have the effect of considerably reducing contributions from points located near the origin or near the z axis ($\theta=0$); in particular, the contribution of the focus will be much lower than Fig. 15 would suggest.

In order to disentangle the various contributions to the reaction cross section, we have calculated the divergence of the quantum flux from the barrier wave contribution to the scattering wave function, as also presented in Fig. 15. Since calculation of the barrier contribution to the wave function involves using an enhanced absorption, we have taken into account this extra absorption in the calculation of the divergence of the barrier flux from Eq. (16). As expected, the barrier contributions for the $\alpha+{}^{40}$Ca and $\alpha+{}^{44}$Ca systems are found to be very similar and localized at the surface of the potential. The barrier contribution, σ_B^{Reac}, to the total reaction cross section can be obtained by integrating the divergence of the barrier flux over space

$$\sigma_B^{\mathrm{Reac}}=\int d^3r\,\nabla\cdot\boldsymbol{j}_B \tag{17}$$

in which unit incident flux has been assumed. More directly, from the barrier wave S-matrix,

$$\sigma_B^{\mathrm{Reac}}=\frac{\pi}{k^2}\sum_{\ell}(2\ell+1)(1-|S_{B,\ell}|^2). \tag{18}$$

The value obtained for the barrier wave contribution to the $\alpha+{}^{44}$Ca reaction cross section (1382 mb) is only 3.5% larger than that obtained for $\alpha+{}^{40}$Ca (1334 mb); this difference is essentially a geometrical effect. It is interesting to calculate in a similar way the internal wave contribution σ_I^{Reac} to the reaction cross section. This is given in terms of the internal wave S-matrix by

$$\sigma_I^{\mathrm{Reac}}=\frac{\pi}{k^2}\sum_{\ell}(2\ell+1)|S_{I,\ell}|^2. \tag{19}$$

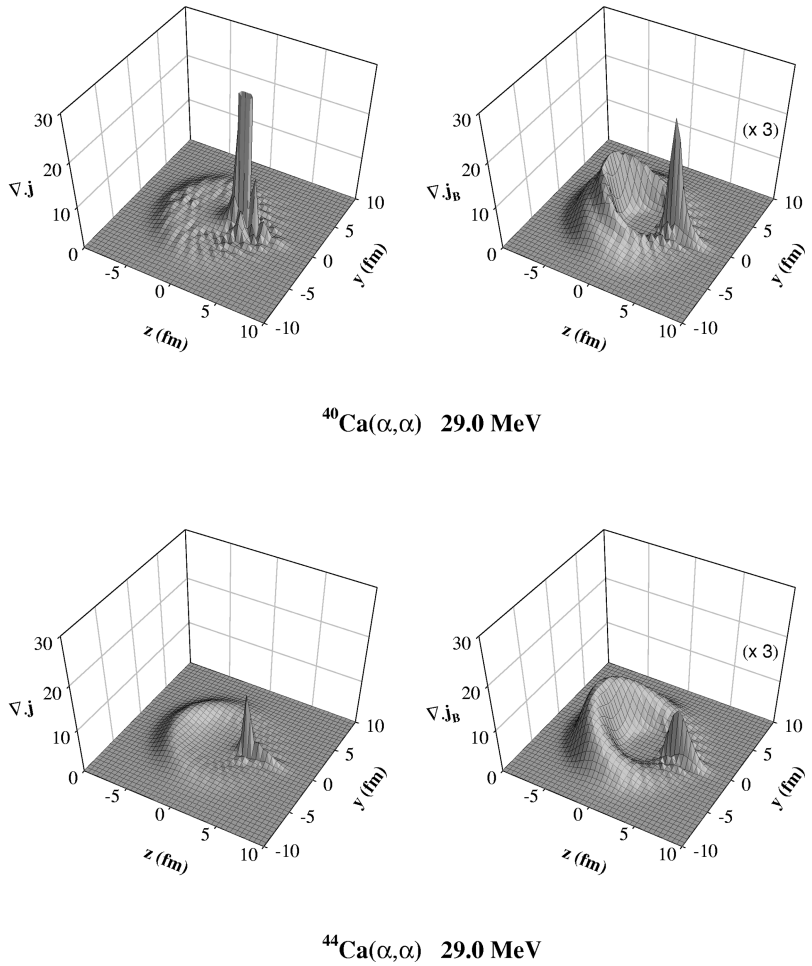

FIG. 15. Divergence of the total (left) and the barrier (right) probability fluxes for the $\alpha+{}^{40}$Ca and $\alpha+{}^{44}$Ca systems at 29 MeV in arbitrary units. The barrier flux has been multiplied by 3 with respect to the total flux.

The internal wave contribution to the reaction cross section is found to be completely negligible in the ^{44}Ca case (0.04 mb). It has, in contrast, a modestly larger value in the ^{40}Ca case (6.8 mb); this last value represents only about 0.5% of the total reaction cross section. It should not be concluded however that the internal wave does not contribute to inelastic scattering processes in low energy $\alpha+{}^{40}$Ca scattering; indeed DWBA calculations of the inelastic differential cross section for excitation of the $J^{\pi}=3^{-},E_x=3.73$ MeV excited state in ^{40}Ca, show that use of a strongly absorbing potential for describing the entrance channel underestimates the inelastic experimental data by more than an order of magnitude at large angles [24], and that the spectacular backward enhancement observed in this inelastic channel is also related to the internal wave contribution, and thus to the focusing properties of the potential.

IV. SUMMARY

We have calculated the quantum probability density and flux for light heavy-ion scattering, taking the $\alpha+{}^{40,44}$Ca and $\alpha+{}^{16}$O systems as illustrative examples. When absorption is incomplete (^{40}Ca and ^{16}O cases), strong focusing is observed at low energy, a phenomenon known for a long time in nucleon-nucleus scattering, and the probability density at the focus is found to reach values much higher than that of the incident wave. Classical calculations then show that the small impact parameter trajectories converge to a point located near the quantum focus. At low energy these trajectories are deflected to large angles and the occurrence of strong focusing thus appears to be correlated with the large angle enhancement (ALAS) observed for these systems. The focus, located well inside the nuclear medium at low energy, moves away from the illuminated side of the target when the energy increases and ALAS is progressively replaced by a rainbow behavior.

Use of a fully quantal procedure makes possible decomposition of the scattering wave function into its barrier and internal wave components, that is, into contributions corresponding respectively to the part of the incident wave reflected at the barrier of the effective potential, and to that crossing the barrier and reemerging after reflection at the innermost turning point. This decomposition confirms the importance of the focus, which dominates the internal wave component, in building up the ALAS phenomenon in $\alpha+{}^{40}$Ca and $\alpha+{}^{16}$O scattering at low energy. Indeed for $\alpha+{}^{44}$Ca, which is dominated by strong absorption and where ALAS is absent, the internal wave probability density is found to be two orders of magnitude lower than that predicted in $\alpha+{}^{40}$Ca. Moreover, the calculation of the quantum flux for the $\alpha+{}^{40}$Ca system shows that the focusing effect is entirely due to the internal wave component of the wave function. Finally, calculation of the divergence of the flux shows that when absorption is incomplete the focal region gives a sizable contribution to nonelastic processes.

[1] M. E. Brandan and G. R. Satchler, Phys. Rep. **285**, 143 (1997).
[2] G. R. Satchler, *Direct Nuclear Reactions* (Clarendon Press, Oxford, 1983).
[3] D. M. Brink, *Semi-classical Methods for Nucleus-Nucleus Scattering* (Cambridge University Press, Cambridge, 1985).
[4] Th. Delbar, Gh. Grégoire, G. Paic, R. Ceuleneer, F. Michel, R. Vanderpoorten, A. Budzanowski, H. Dabrowski, L. Freindl, K. Grotowski, S. Micek, R. Planeta, A. Strzalkowski, and K. A. Eberhard, Phys. Rev. C **18**, 1237 (1978).
[5] D. A. Goldberg and S. M. Smith, Phys. Rev. Lett. **29**, 500 (1972).
[6] J. Albinski and F. Michel, Phys. Rev. C **25**, 213 (1982).
[7] F. Michel, J. Albinski, P. Belery, Th. Delbar, Gh. Grégoire, B. Tasiaux, and G. Reidemeister, Phys. Rev. C **28**, 1904 (1983).
[8] I. E. McCarthy, Nucl. Phys. **11**, 574 (1959).
[9] I. E. McCarthy, Nucl. Phys. **10**, 583 (1959).
[10] I. E. McCarthy, Phys. Rev. **128**, 1237 (1962).
[11] K. A. Amos, Nucl. Phys. **77**, 225 (1966).
[12] I. E. McCarthy, *Introduction to Nuclear Theory* (John Wiley, New York, 1968); *Nuclear Reactions* (Pergamon Press, Oxford, 1970).
[13] A. J. Kromminga and I. E. McCarthy, Nucl. Phys. **24**, 36 (1961).
[14] R. S. Mackintosh, A. A. Ioannides, and S. G. Cooper, Nucl. Phys. **A483**, 173 (1988).
[15] R. S. Mackintosh, A. A. Ioannides, and S. G. Cooper, Nucl. Phys. **A483**, 195 (1988).
[16] R. S. Mackintosh, S. G. Cooper, and A. A. Ioannides, Nucl. Phys. **A476**, 287 (1988).
[17] R. da Silveira, S. Klarsfeld, A. Boukour, and Ch. Leclercq-Willain, Phys. Rev. C **51**, 1572 (1995).
[18] K. W. Ford and J. A. Wheeler, Ann. Phys. (N.Y.) **7**, 259 (1959).
[19] R. C. Fuller, Phys. Rev. C **12**, 1561 (1975).
[20] D. M. Brink and N. Takigawa, Nucl. Phys. **A279**, 159 (1977).
[21] M. S. Hussein and K. W. McVoy, Prog. Part. Nucl. Phys. **12**, 103 (1984).
[22] H. Abele and G. Staudt, Phys. Rev. C **47**, 742 (1993).
[23] H. P. Gubler, U. Kiebele, H. O. Meyer, G. R. Plattner, and I. Sick, Nucl. Phys. **A351**, 29 (1981).
[24] F. Michel and R. Vanderpoorten, Phys. Rev. C **16**, 142 (1977).
[25] T. Wada and H. Horiuchi, Phys. Rev. Lett. **58**, 2190 (1987).
[26] H. Horiuchi, in *Trends in Theoretical Physics*, edited by P. J. Ellis and Y. C. Tang (Addison-Wesley, Reading, MA, 1991), p. 277.